The Role of Iron in the Formation of Porosity in Al-Si-Cu–Based Casting Alloys: Part I. Initial Experimental Observations

J.A. TAYLOR, G.B. SCHAFFER, and D.H. StJOHN

Outbreaks of interconnected porosity in industrial Al-Si–based alloy castings have, on occasion, been attributed to variations in metal chemistry rather than to changes in process parameters. This work identifies the role that iron plays in porosity formation and reports a threefold effect in an Al-5 pct Si-1 pct Cu-0.5 pct Mg alloy. In addition to a detailed analysis of casting porosity profiles, metallographic and thermal studies also point to inadequacies in the existing theories regarding the role of iron and suggest that a new theory is required to understand the observed behavior.

I. INTRODUCTION

MANY commercial aluminum foundries occasionally experience serious outbreaks of porosity in low-pressure and gravity die castings that normally cast well and with low reject rates. Many process and/or design factors, such as local thermal conditions,[1] feeding capacity,[2] and applied pressure[3] are known to affect porosity formation. Metal-related factors, including dissolved hydrogen,[4] inclusions,[5,6] modifying elements,[7,8] and other minor element additions[9] can also influence porosity formation. These have been reviewed by Taylor.[10] The cause of sporadic porosity outbreaks in the foundry is sometimes deemed to be metal related and may be attributed to a particular batch of alloy, even though it is within chemical specification.

Although there is anecdotal evidence that iron has a negative influence on porosity formation, there has been little prior research on the specific effect of iron. An exception is the work of Iwahori *et al.*,[11] who found that larger riser sizes were required in order to avoid the formation of a shrinkage-porosity defect in castings of an AC2B alloy (Al-6.8 pct Si-3.2 pct Cu) as the iron level was increased above 0.5 pct (all compositions are given in wt pct). However, they did not propose a mechanism. Two theories have been proposed by others to account for the deleterious effect of iron on porosity.[12,13] Both imply that the level of porosity should increase monotonically with iron content, but this is not consistent with foundry experience.

The current work, based on the doctoral dissertation by Taylor,[14] describes a systematic study into the effect of iron on porosity in the Al-Si-Cu-Mg alloy AA309 (the Australian equivalent to US code 355). This article presents the results from an experimental casting program, which point to the shortfalls in the current theories. Two companion articles propose a mechanism consistent with observations based on phase-diagram characteristics[15] and microstructural development.[16]

J.A. TAYLOR, formerly Doctoral Student, is Senior Research Fellow, CRC for Alloy and Solidification Technology (CAST), Department of Mining, Minerals and Materials Engineering, The University of Queensland. G.B. SCHAFFER, Reader, and D.H. StJOHN, Professor, are with CAST, Department of Mining, Minerals and Materials Engineering, The University of Queensland, Brisbane, QLD 4072, Australia.

Manuscript submitted March 27, 1998.

II. EXPERIMENTAL

A total of 94 cylindrical-shaped AA309 alloy castings were made using a variant of the improved low-pressure (ILP) casting process originally developed by Comalco Aluminium Limited (Brisbane, Australia). The ILP process is a precision sand casting process that utilizes an assembly of resin-bonded mold components and thermal cores (chills). The mold assembly is filled by underpouring and is then inverted prior to solidification. The ILP process was selected because it is readily used in a laboratory foundry, is easily modified, and provides a degree of comparison to the low-pressure die casting process.

Details of the dimensions, assembly, and operation of the laboratory-variant ILP process used in the present work are shown in Figure 1. The mold sections (four blocks plus a cylindrical core) were made from a Pepset resin-bonded silica sand (of American Foundry Standard 60 grade). The chill was made of a graphite spray-coated 6063 aluminum alloy and was molded into one of the sand blocks (uppermost in the pouring orientation). The mold blocks and core were clamped together into an invertable cradle. Manual pouring of the melt into the down sprue allowed an essentially underpoured filling of the mold cavity to occur, in which the influence of the chill was retarded until the mold was completely full. Upon completion of pouring, the cradle and mold assembly were inverted to allow gravity-fed, quasi-directional solidification to take place.

A single batch of a low-iron (0.10 pct), primary AA309 ingot was used throughout as the base alloy. A standard metal preparation regime was followed for each casting (Figure 2). For each casting, approximately 4 kg of metal was melted in a clay-bonded graphite crucible using a 20 kV induction furnace. In order to minimize any composition differences between casts arising from segregation effects within ingots, each charge was based on a symmetrically halved as-received ingot. Iron additions (when required) were made at 740 °C using *ALTAB* (London Scandinavian Metallurgical Company) *Fe* compacts (75 pct Fe, 15 pct Al, and 10 pct Na-free flux) and were held for 10 minutes. No grain refiners or modifiers were added.

Each melt was degassed, using argon, for 10 minutes at a flow rate of approximately 5 L/min. Following degassing, the melts were skimmed and then returned to a pouring temperature of 745 °C. Melt temperatures above 750 °C

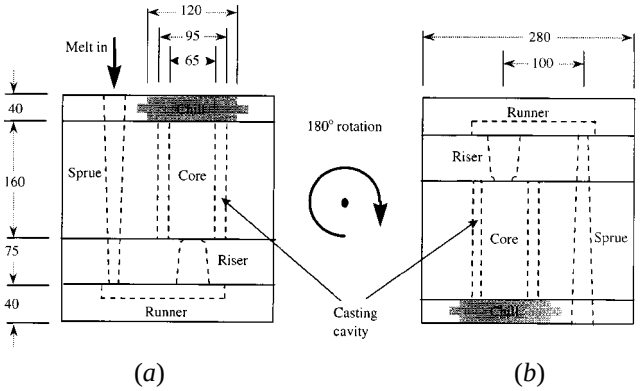

Fig. 1—The ILP mold assembly used for producing the cylindrical test castings, showing (*a*) the pouring mode orientation and (*b*) the inverted solidification mode orientation. The key dimensions of the assembly and casting are expressed in millimeters. The sand block dimension into the page is approximately 305 mm. The riser diameter varies from 45 to 50 mm along its length. The chill has a locating rim of 10 × 15-mm cross section and has a rebate 20-mm deep (not shown) to locate the central sand core. The whole assembly is clamped together in an invertable cradle (not shown). The clockwise inversion, as shown above, results in the loss of molten metal from the sprue and runner system only.

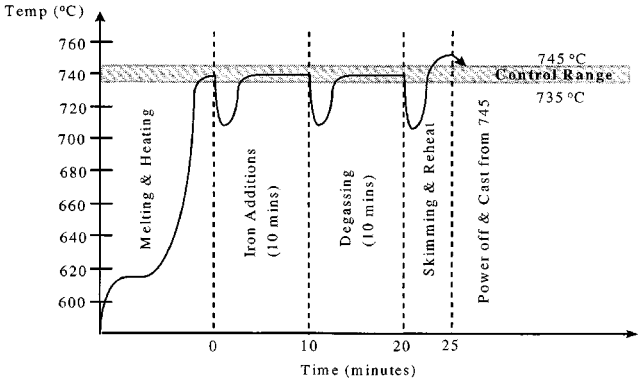

Fig. 2—Schematic representation of a typical melting and alloying regime for the experimental casts. The actual minimum temperatures varied, but rarely fell below 700 °C.

were avoided, since these are known to cause changes to the aluminum-oxide phase type (from γ-Al_2O_3 to α-Al_2O_3), which, in turn, favors the formation of different iron-containing phases (β-Al_5FeSi and α-$Al_{15}Fe_3Si_2$, respectively).[17] All casts were manually poured. A pouring temperature of 745 °C allowed the melt of approximately 610 °C (near the liquidus temperature) to reach the chill end of the mold. Inversion of the mold assembly occurred within 2 to 3 seconds after pouring ceased.

The cylindrical test castings were 160-mm long, with an o.d. and i.d. of 95 and 65 mm, respectively (Figure 1). Three series of castings were produced for investigation. Four different casting configurations (using combinations of one or two risers, with or without the end chill) were employed during stage I, and these are shown in Figure 3. The stage I castings were made using two different iron levels (the base composition of 0.1 pct Fe and an upper iron level of 1.0 pct). During stage II, the one riser–without chill configuration (1RNC) (Figure 3) was selected, and castings with intermediate iron levels (nominally, 0.25, 0.40, 0.55, 0.70, and 0.85 pct) were produced in a random sequence.

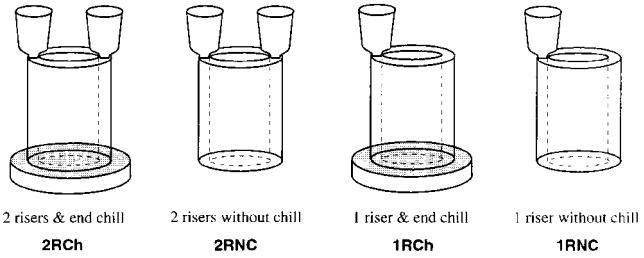

Fig. 3—The four configurations used to produce the cylindrical test castings during stage I of the experimental program and the notation used to describe them. The casting dimensions are shown in Fig. 1.

Finally, in stage III, castings were produced at 0.4 pct Fe in the two riser with chill configuration (2RCh). For each alloy/configuration combination in the three stages, a minimum of four castings was produced.

Each casting was sectioned into 32 segments (eight 20-mm-deep cylindrical rings each divided into quadrants), as shown in Figure 4. The quadrants were designated A, B, C, and D (where B and D were beneath the risers in the two-riser system and B was beneath the riser in the single-riser system). A numeral from 1 to 8, following the letter, designates the ring number; 1 is closest to the chill, and 8 is closest to the riser.

The densities of these segments were determined using Archimedes' method, with ethanol as the suspending medium. A precision research balance (resolution 0.00001 g) was used throughout. The porosity of each segment (*P*, expressed in volume percent) was calculated by comparing the measured segment density and the theoretical alloy density (the latter being derived using the rule of mixtures on the estimated proportions of all phases present in the microstructure and the published densities of the intermetallic phases[18,19]). The calculated maximum error for the measured porosity of an individual segment arising from the overall experimental technique was found to be *P* pct ± 0.1 pct for all *P* levels ($\pm 3\sigma$, *i.e.*, >99 pct confidence). Average porosity values for whole castings were then calculated using

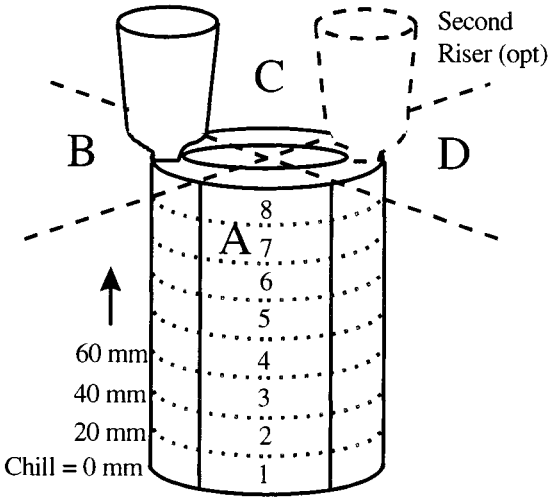

Fig. 4—The cylindrical casting showing the segment designation nomenclature and the distances of ring parting lines from the 'chill' end. The casting dimensions are shown in Fig. 1.

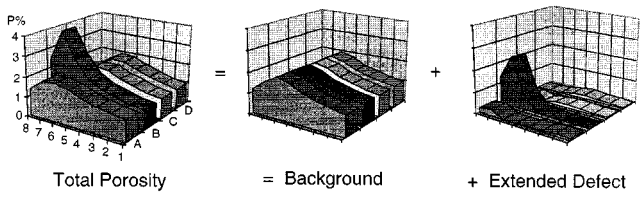

Fig. 5—A simplified representation of a measured porosity profile and the manner in which it was divided into two contributions, termed background and extended defect. This example is the actual profile for a 1RNC casting made from AA309 with 1.0 pct Fe. The *x* and *y* scales locate the individual segment positions and the *z* scale represents porosity (vol pct), *e.g.*, maximum porosity level of 4 pct is at B7.

mass-weighted averages of the *P* values for the 32 component segments. Since the errors in measuring individual segment porosity values are expected to be normally distributed, the effect of averaging these porosity values to obtain a value for the whole casting will be to reduce the overall error to much less than ± 0.1 pct.

A porosity profile was determined for each casting using the 32 individual segment values (an example is shown in Figure 5). Each porosity profile was further split into two components, a background value and an "extended-defect" value, the latter being essentially the size of the localized shrinkage defect above the general background porosity level. For any given condition (*i.e.*, alloy and cast configuration), average values of total porosity, background porosity, and extended-defect size were calculated from the four or more representative castings. The statistical significance of the data was analyzed using the Student's *t*-test and the *F*-test.

The type, size, and spatial distribution of both the porosity and the intermetallic phases present were examined by optical microscopy of unetched samples. The size and amounts of the iron-containing intermetallics (β plus π) were quantified using eight fields of 500×500 μm for each sample. The length of the largest intermetallic particle observed in each field was measured and the average value was determined (L_{max}). An estimate of the average number of particles per field area (N) is given by

$$N = (H_{avg} + 1)\,(V_{avg} + 1) \qquad [1]$$

where H_{avg} and V_{avg} are the average number of particles intersecting the horizontal and vertical centerlines of a field, respectively. The additions of unity avoid a zero value for *N*.

Cast samples for composition analysis were prepared from each melt. Chemical analysis was carried out by spark emission spectroscopy, while hydrogen analysis was by the LECO* nitrogen carrier fusion technique. Several cylindrical castings were also produced with embedded type-K thermocouple wires. Data were acquired at a scan rate of 10 Hz using the LabTech Notebook Software running on a PENTIUM* PC. Various thermal parameters, including local solidification times, cooling rates, thermal gradients, and times/temperatures of phase formation, were obtained from this information.

*LECO is a trademark of LECO Corporation, St. Joseph, MI.

*PENTIUM is a trademark of Intel Corp., San Jose, CA.

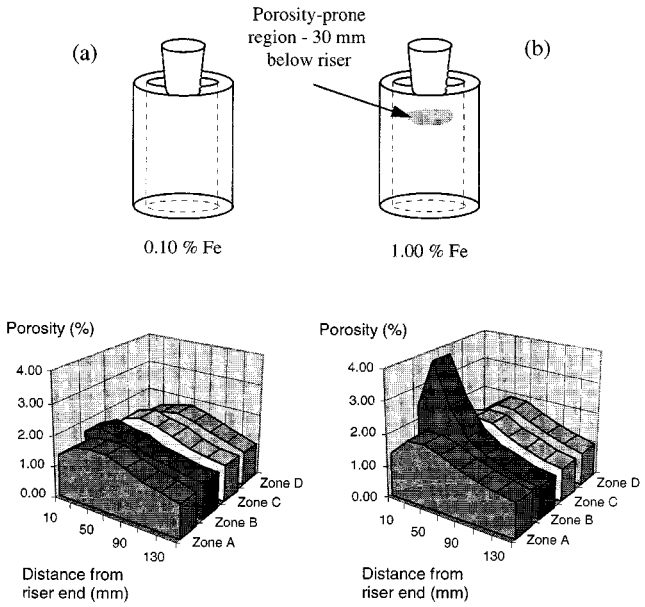

Fig. 6—The effect of (*a*) 0.10 pct Fe and (*b*) 1.00 pct Fe on the formation of porosity in AA309 alloy in the single riser without chill casting configuration. The upper drawings illustrate defect formation in the castings. The lower drawings are representative porosity profiles. Zone B is the riser quadrant, while zones A, C, and D are the quadrants at -90, $+90$, and $+180$ deg from B, respectively. Note that the development of a major extended defect occurs around B7 (30 mm from riser end) in the high iron alloy.

III. RESULTS

The porosity profiles that were determined for each of the individual castings from stage I were initially compared visually. From this inspection, it was immediately apparent that, although absolute levels of porosity varied from casting to casting and from segment to segment, the shapes of the obtained profiles displayed a consistency of basic shape and generally showed smooth transitions between the porosity values of adjacent segments. This provided for a high degree of confidence in the results that follow.

In three of the four configurations used in stage I of the casting program, *i.e.*, two risers with chill (2RCh), one riser with chill (1RCh), and two risers without chill (2RNC), there was no significant change in either profile shape, total casting porosity, or any substantial evidence of the formation of any localized shrinkage defects when the iron level was increased from the base level of 0.1 pct up to 1.0 pct. However, in the castings made using the fourth configuration, *i.e.*, 1RNC, a major localized region of shrinkage porosity became evident in the castings with the higher iron level, even although the average total casting porosity did not change significantly. These shrinkage-defect regions were typically focused at the B7 segment (below the riser) and, to a lesser extent, were also present in the adjacent segments, *e.g.*, A7, B6, C7, *etc.*, and are shown in Figure 6. Although the size of this so-called "extended defect" varied from cast to cast, the Student's *t*-test indicated that the mean of the high-iron extended-defect size is significantly different (to >95 pct confidence) from the mean size of the equivalent "no-defect" regions in the corresponding low-iron castings.

Figure 7 shows the average calculated contributions of the background porosity and the extended-defect size to the

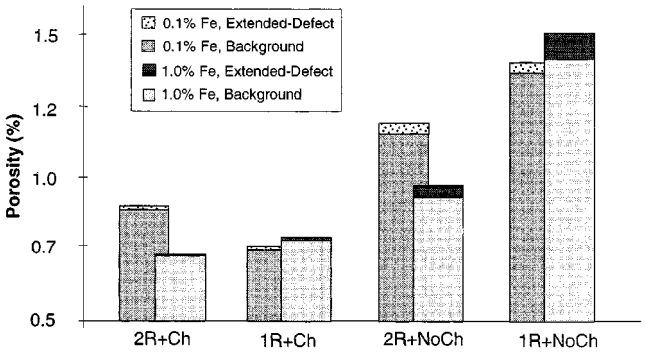

Fig. 7—The contributions toward the total casting porosity (four-cast averages) from both the extended defect and the background in the four casting configurations of stage I at both 0.10 pct Fe and 1.00 pct Fe contents.

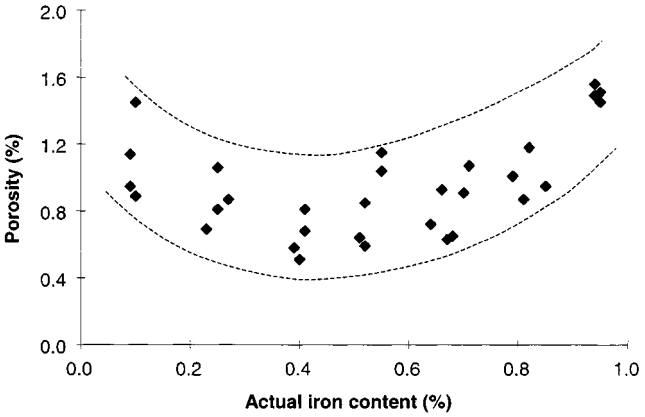

Fig. 8—The average total porosity level *vs* the actual iron content for each stage II casting (mass-weighted average of 32 component segments) in the 1RNC configuration. The dashed lines show approximate ranges only. The validity of the trends was confirmed by statistical analysis of the data. See text for details.

total casting porosity for the four stage I casting configurations at the two iron contents. Besides further illustrating the previous findings, this figure also shows that, for both low and high iron levels, the overall porosity levels increased as the casting configuration deteriorated from the original optimum design of 2RCh to the poorest condition of 1RNC. This is to be expected, since a reduction in feeding capacity (two risers to one riser) or a lowering of the thermal gradient and cooling rates (resulting from the removal of the chill) are both deleterious casting actions.

The appearance of the localized shrinkage defect (*i.e.*, extended defect), in the vicinity of casting segment B7 at 1.0 pct Fe content in the 1RNC configuration, raised the issue of the development of this defect at intermediate iron contents. Iron contents of 0.25, 0.40, 0.55, 0.70 and 0.85 pct were selected for investigation during stage II. Two factors are apparent from the resultant porosity profiles and their averaged values of background porosity and extended-defect size.

First, as the iron content increases, the total porosity values initially decrease, until a minimum value is reached at 0.4 pct Fe, after which further increases in iron result in increased total porosity levels (Figure 8). This minimum is evident despite the cast-to-cast variations in measured porosity. The Student's *t*-test indicates that the mean porosity at 0.4 pct

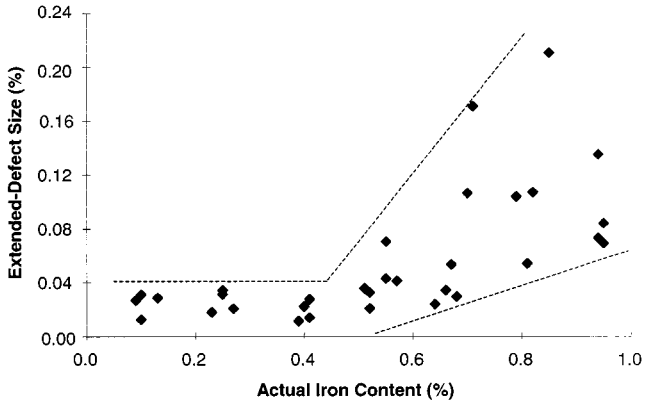

Fig. 9—The size of the extended defect *vs* the actual iron content for each of the stage II castings (mass-weighted average of 32 component segments) in the 1RNC configuration. The dashed lines show the approximate ranges. Student's *t*-tests and *F*-tests confirm that there is a high probability that the trends are statistically significant. See text for details.

Fe is significantly different (>95 pct confidence) from the mean values at either 0.1 or 1.0 pct Fe, while an F-test indicates that the variance is similar at all iron levels except 1.0 pct, where it is much lower. This suggests the minimum observed at 0.4 pct is real and that the suggested scatter bands are valid. There is an inherent variability in the castings, presumably resulting from the casting process rather than the alloy composition. This variability may be due to differences in entrained oxide levels, known to affect porosity formation.[5,6,20] Oxide formation was only controlled by adoption of standard melt practices and was not measured to determine its variability from cast to cast. Hydrogen is not a major influence on these observed porosity effects in the experimental castings (as detailed subsequently).

Second, the stage II castings indicate that the formation of the extended defect around segment B7 does not occur until iron contents exceed 0.4 pct (Figure 9). Statistical analysis indicates that change in the mean extended-defect size and the variance between the lower iron contents (0.1, 0.25, and 0.4 pct) and the higher iron contents (0.7, 0.85, and 1.0 pct) are significant to approximately 90 and 95 pct confidence, respectively. The implied difference between the lower iron results and those of 0.55 pct Fe in Figure 8 is slightly less certain (different mean, 90 pct confidence; different variance, 70 to 80 pct confidence), but is still real. This means that, as the iron content increases above a critical 0.4 pct value, the formation of extended defects becomes both more intense and more frequent, as evidenced by a widening of the scatter band and the increase in the minimum measured level. The variable scatter at the lower end of the supercritical iron range suggests that both good and bad castings were made, whereas higher supercritical iron contents produced only poor castings. Several of these high-iron castings showed evidence of interconnected porosity leakage paths in some B7 segments.

Although the 2RCh configuration had shown no evidence of extended-defect formation at high iron levels during stage I, it was not known if the minimum total porosity would occur at 0.4 pct. To answer this question, the stage III castings were produced. Porosity values (background and extended defect) for these 0.4 pct Fe castings in the 2RCh configuration were compared to those of the 0.1 and 1.0 pct Fe castings

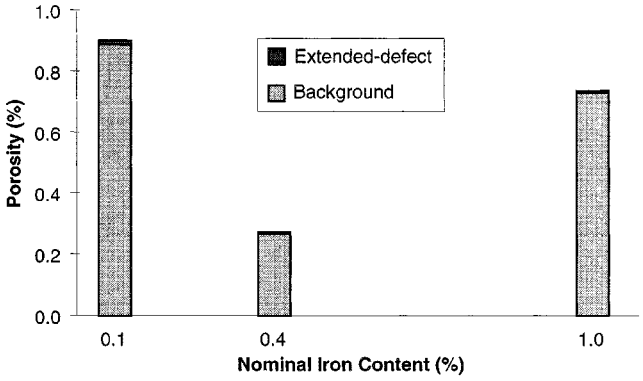

Fig. 10—The average contributions of background porosity and extended-defect size to the total casting porosity in AA309 alloy castings of three different iron contents produced in the 2RCh configuration. The extended-defect sizes are negligible and the lowest total porosity value was observed at 0.4 pct Fe. A Student's *T*-test confirms that there is a high probability that there is a statistically valid difference in mean values, indicating that the minimum shaped curve is real. See text for details.

in the same configuration. These data are summarized in Figure 10 and show that, although this configuration does not favor extended-defect formation at high iron levels, a minimum total porosity value does occur at an intermediate iron content. However, it is not possible to definitively determine from these results whether the actual minimum value occurs exactly at 0.4 pct Fe or at some other iron content. The mean porosity value obtained at 0.4 pct Fe differs significantly from the mean values at both 0.1 and 1.0 pct Fe, to a confidence level of at least 90 pct.

Optical metallography revealed that significant porosity only formed at iron contents greater than 0.4 pct and that it was concentrated around the B7 region of the castings. Figure 11 shows the pore morphology in the B7 segments of the stage I castings. At the low iron content (0.1 pct), the predominant pore morphology is discrete individual pores with rounded-to-elongated shapes. This was invariant with changing casting configurations. However, at the high iron content (1.0 pct), the predominant morphological form is interdendritic sponge porosity (which becomes increasingly more interconnected as the casting conditions are degraded).

Figure 12 shows the trends in porosity of the B7 segment with changing iron content in the 1RNC casting configuration (stage II). When the iron concentration is below 0.4 pct, the porosity remains unconnected, although the morphological form shifts from discrete individual pores to small sponge regions at 0.25 and 0.4 pct Fe. At higher iron contents, sponge porosity is the predominant form and becomes increasingly interconnected, such that leakage paths are formed.

Two iron-containing intermetallic phases were evident in the microstructures of the AA309 alloy. These are β-Al_5FeSi and π-$Al_8Mg_3FeSi_6$. The former occurs in the interdendritic and intergranular regions as platelets (appearing as needles in metallographic sections) and the latter occurs as either a Chinese-script phase or an indefinite-shaped peritectic phase growing from and/or coating the β platelets. In general, apart from the 0.1 pct Fe alloy in which there was more Chinese-script π phase than β, the principal phase at all other iron contents is β. The presence of β platelets at both low (0.1 pct) and high (0.85 pct) iron contents in the AA309 alloy

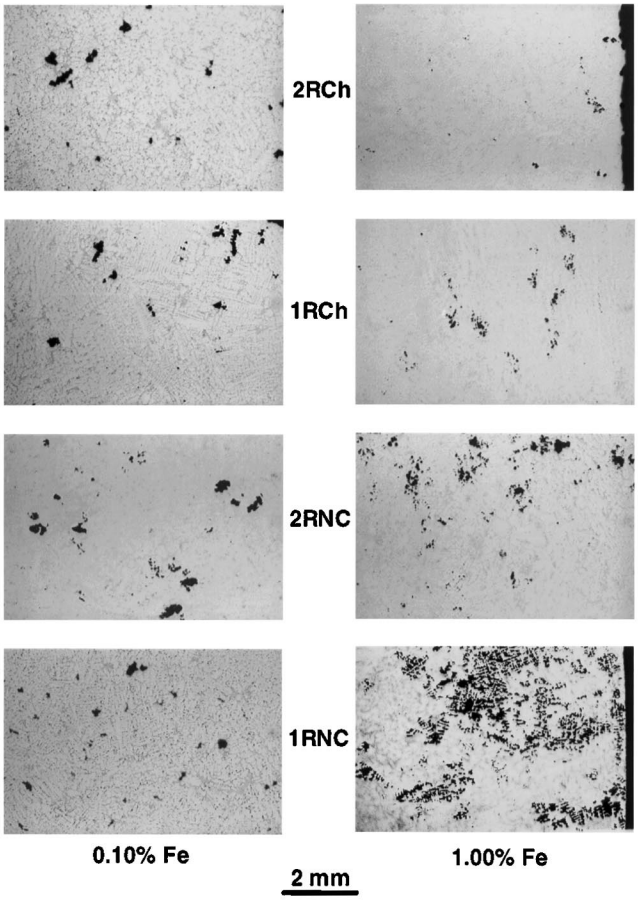

Fig. 11—Optical micrographs of porosity in selected B7 segments of the stage I castings at both the low and high experimental iron contents in the four casting configurations.

is highlighted in the micrographs of Figure 13. The distribution of the β platelets within the microstructure was inhomogeneous, because of variations in the size and location of the interdendritic Al-Si eutectic regions where the β phase forms. The maximum observed length of the iron-containing intermetallic particles and the average number of these particles per field, in the defect-prone B7 segments of the 1RNC castings, increased linearly as the iron content increased.

Chemical analysis of all melts from stages I and II gave an average composition of the AA309 alloy castings as 5.12 pct Si, 1.18 pct Cu, and 0.50 pct Mg. The iron levels were generally lower than the target composition by approximately 0.05 pct. Hydrogen analyses showed that bulk hydrogen contents ranged from 0.03 to 0.20 ppm (average 0.08, $1\sigma = 0.03$). These contents are relatively low, are consistent with the application of the standard degassing method, and indicate that shrinkage (rather than hydrogen gas) is likely to be the dominant cause of porosity in the experimental castings. This was confirmed by comparing the hydrogen content to the measured total porosity and extended-defect size for stage I and II castings. No correlations were observed. The hydrogen concentration was also independent of iron content.

Average local cooling rates for individual segments were defined in terms of the time taken from the point at which solidification starts in the chill region (610 °C) until the segment temperature drops to 500 °C (the start of the final

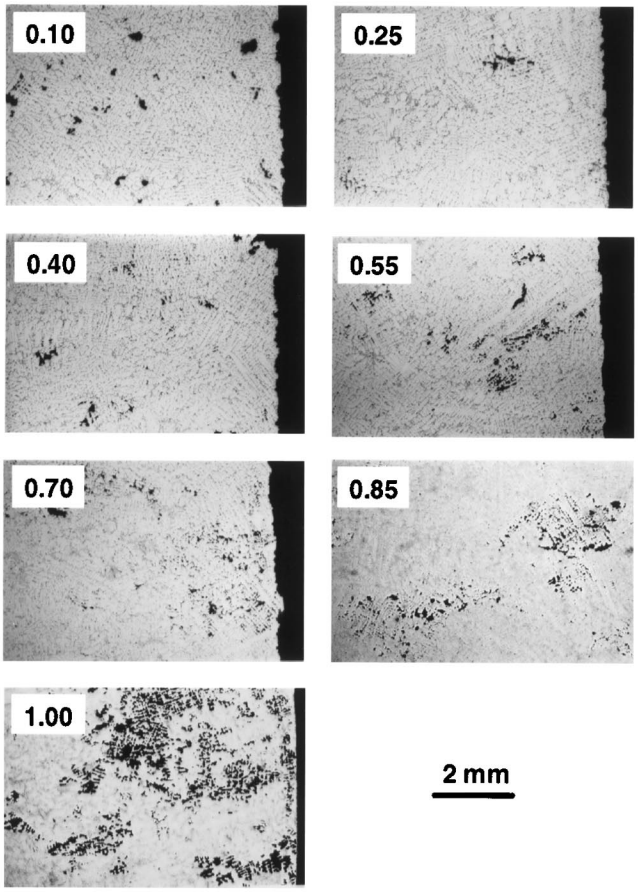

Fig. 12—Optical micrographs of the porosity found in selected B7 segments of stage II castings in 1RNC configuration. The numbers on the micrographs represent the iron contents expressed in weight percent.

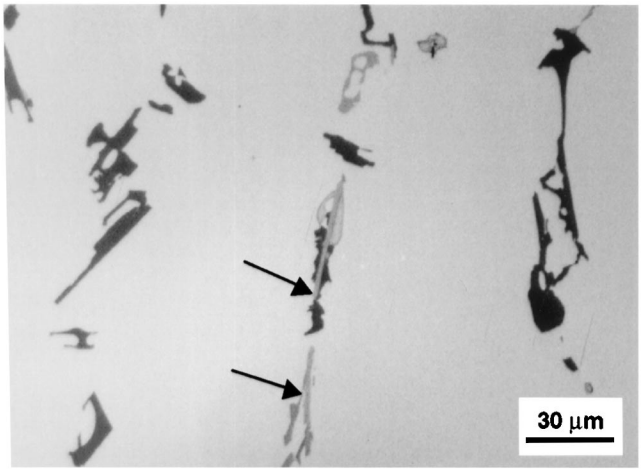

(*a*)

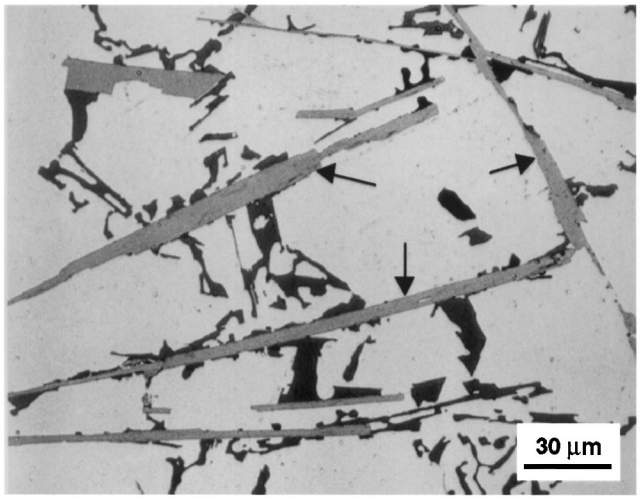

(*b*)

Fig. 13—Optical micrographs showing the β-Al_5FeSi platelets (arrowed) in the microstructures of AA309 alloy containing (*a*) 0.1 pct Fe and (*b*) 0.85 pct Fe. Other phases, notably silicon, can be seen at the surface of the β platelets.

quarternary reaction defined by Backerud *et al.*[21]). For both stage I and II castings, the cooling rate for any given segment in any given configuration is essentially independent of iron content. Averaged values between the castings are, therefore, used.

The differences in local cooling rates at any segment between the four stage I casting configurations were primarily a function of the chill. At the "chill" end (segment B1), there was an order-of-magnitude difference between the chill and no-chill conditions, *i.e.*, 7.9 °C/s (1RCh) and 0.40 °C/s (1RNC). At the "nonchill" end (segments B7 and B8), however, the differences in cooling rates were minimal; *i.e.*, 0.38 °C/s (1RCh, segment B8) and 0.30 °C/s (1RNC, segment B8) and 0.44 °C/s (1RCh, segment B7) and 0.31 °C/s (1RNC, segment B7).

Although the thermal gradients are relatively low and flat in the 1RNC configuration (between 0.1 °C/mm and 0.6 °C/mm at B7 compared to 0.3 °C/mm to 1.3 °C/mm at B1), there is, nevertheless, nominally directional solidification toward the riser. Thermocouples in the riser body and the riser neck indicate that solidification finishes in the riser body without any evidence of freezing off in the neck region, *i.e.*, time to 100 pct solidification at $R_{body} > R_{neck} >$ B8 > B7. This suggests that the defect-prone B7 region solidifies under essentially directional conditions. It is interesting to note that, although the thermal gradients at B1 in the chilled castings were an order of magnitude greater than those at B1 in the no-chill castings, the gradients around the defect-prone B7 region were only slightly improved by the presence of the chill (0.4 °C/mm to 0.6 °C/mm compared to 0.1 °C/mm and 0.6 °C/mm (no-chill)).

Backerud *et al.*[21] suggested that seven reactions should occur during solidification of an equivalent alloy (alloy C355.2). These are

(1) Liquid → Al dendrite formation
(2) Liquid → Al + Al_5FeSi
(3) Liquid → Al + Si + Al_5FeSi
(4) Liquid + Al_5FeSi → Al + Si + $Al_8Mg_3FeSi_6$
(5) Liquid → Al + Si + Mg_2Si + $Al_8Mg_3FeSi_6$
(6) Liquid → Al + Al_2Cu + Al_5FeSi + Si
(7) Liquid → Al + Al_2Cu + Si + $Al_5Mg_8Cu_3Si_6$

Figure 14 shows these reactions on a typical cooling curve and its derivative, where reactions 3 and 4 are superimposed on each other, as are reactions 5 and 6. Because of the low Cu and Mg contents in the AA309 alloy, reactions 5 through 7 are relatively insignificant and occur much too late in the

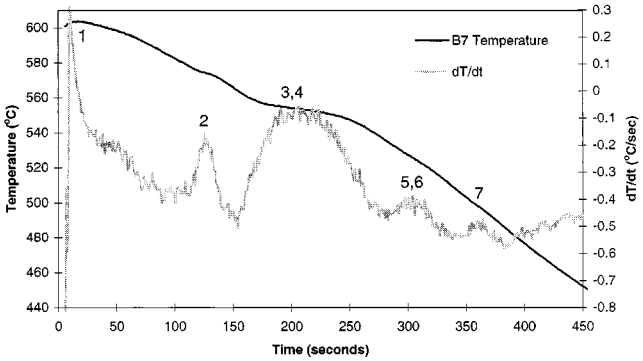

Fig. 14—Typical cooling curve for the B7 segment (1RNC, 0.7 pct Fe) showing the inflections/peaks associated with the seven reactions described by Backerud *et al.*[21] See text for details.

solidification sequence to provide the level of shrinkage required for major defect formation.

Reaction 2 (the formation of Al-Al_5FeSi) only occurred in stage I in the high-iron (1 pct) alloys. The size of the peak increased as the cooling rates decreased (*i.e* favored by the no-chill conditions and increased distance from the chill end). During stage II, reaction 2 did not occur at all at the lower iron levels of 0.1 to 0.4 pct, but became prominent at 0.55 pct Fe and above, occurring earlier and at higher temperatures as the iron content increased toward 1.0 pct (Table I). Reaction 2 was also affected by the local cooling rate (*i.e.*, casting location), with slow cooling rates resulting in higher temperatures of formation and longer delays until maximum phase formation occurred.

Eutectic silicon formation in the AA309 alloy (reactions 3 and 4) occurs between 560 °C and 550 °C and is essentially independent of iron content at all cooling rates. Since Al-Al_5FeSi formation is extremely dependent on iron, the interval between these two regimes is also iron-content dependent. For any given cooling rate, both the temperature interval and time interval increase as the iron content increases. The average values of the temperature interval for iron contents >0.55 pct are shown in Table II.

IV. DISCUSSION

The results indicate that iron exhibits a strong threefold influence on porosity and shrinkage-defect formation in alloy AA309 (in the unmodified, nongrain-refined condition). The three aspects of this iron-porosity effect are

(1) the development of a localized shrinkage-porosity defect, at iron contents above approximately 0.4 pct, in castings produced under poor cooling and feeding conditions;
(2) the occurrence of a configuration-independent minimum total porosity and minimum background porosity values at this same critical iron content; and
(3) a change in pore morphology from discrete isolated pores of rounded and elongated shape to regions of spongy interdendritic porosity at iron contents above 0.1 pct.

Table I. Temperatures of Formation of Pre-Eutectic β Phase at Three Locations within Stage II Castings with Iron Contents from 0.55 to 1.00 Weight Percent

	Temperature (°C)		
Iron (Wt Pct)	B1 Chill End	B7 Defect Zone	B8 Riser End
0.55	558	569	572
0.70	569	575	580
0.85	582	581	578
1.00	584	586	587

Table II. Temperature Intervals between the Formation of Pre-Eutectic β Phase and Eutectic Al-Si at Three Locations within Stage II Castings with Iron Contents from 0.55 to 1.00 Weight Percent

	Temperature (°C)		
Iron (Wt Pct)	B1 Chill End	B7 Defect Zone	B8 Riser End
0.55	11	12	17
0.70	17	20	23
0.85	26	26	29
1.00	31	32	33

The iron-porosity relationship is not monotonic. Indeed, iron is not solely a detrimental element. Up to the critical iron content, there are beneficial effects. Thereafter, there is a deleterious contribution from iron toward porosity formation, but it is only apparent under poor casting conditions. The value of 0.4 pct Fe, at which the minimum in porosity occurs, also represents the highest iron value without any evidence of reaction 2. It is also noteworthy that the value of 0.4 pct Fe is consistent with industrial experience with the AA309 alloy, which has shown that occasional outbreaks of high reject rates for "leakers" in cylinder heads may be associated with iron levels slightly greater than this.[22]

Although the deleterious role of iron on castability and porosity formation has been noted by others,[11,12,23] the suggestion that there might also be a beneficial effect of iron on porosity formation under certain conditions has not been reported previously. To date, only two basic mechanisms have been proposed in the literature to account for the deleterious role of iron in porosity formation in aluminum alloys. The first of these can be termed the "restricted feeding theory" and the second, the "pore nucleation theory."

The former theory, as originally proposed by Mascre[12] and more recently by others,[11,23] suggests that the β-Al_5FeSi intermetallic platelets restrict feeding. Since the platelets form in the interdendritic channels during solidification, they cause physical restrictions to the movement of compensatory feed liquid. Regions undergoing shrinkage cannot be fed adequately and porosity is likely to form as a result. Iwahori *et al.*[11] introduced the concept of a metal feeding-limit temperature below which feeding is restricted and shrinkage defects arise. For alloy AC2B (approximately 6.8 pct Si and 3.2 pct Cu), the limiting temperature was found to be constant at 570 °C, up to iron levels of 0.5 pct, but to increase thereafter with increasing iron content. This trend is similar to the onset of Al-Al_5FeSi formation above 0.4 pct Fe noted here and to the increasing formation temperature as the iron content increases. However, an increase in the β phase *per se* cannot be the cause for increased shrinkage porosity, since the present observations show that β is present in the

microstructures even at iron contents below 0.4 pct (Figure 13). This suggests that it is the origin of the β phase, rather than the nature of and/or the quantity and size of the β phase itself, which is likely to influence the formation of porosity. The existing restricted-feeding theories are, therefore, not capable of explaining the reduction in porosity levels observed as the iron content increases to 0.4 pct.

The second theory, as proposed by Roy *et al.*,[13] suggests that β platelets are active pore nucleation sites and also physically constrain the growth of the pores and, so, influence the ultimate pore shapes. The implication is that, since the size and amount of the β platelets increase with iron content, there should also be a monotonic increase in the number of pores.

The primary objection to the pore nucleation theory is the observation that, at least up to iron levels of 0.4 pct, there does not appear to be an increase in the actual number of pores observed in any given area. Moreover, the presence of large clusters of β platelets within a particular area of the microstructure does not of itself lead to the formation of more pores. It might be argued that the breakdown of the larger elongated pores observed in the 0.1 pct Fe castings to the smaller spongy pore regions observed at higher iron contents is evidence of increased pore nucleation (Figures 11 and 12). However, these spongy pore regions are three-dimensional objects rather than the two-dimensional planar artifacts observed by optical microscopy. That is, the sponge regions may be single pores that follow the contours of the three-dimensional dendrite arms through several grains in a tendril-like manner. Although the pore-nucleation aspect of this theory also appears incapable of explaining the observations of the present investigation, the growth-restricting/shape-forming aspect of the theory does, nevertheless, appear to be consistent with the current results.

The experimental data illustrate that the iron-porosity relationship is somewhat more complex than a simple incremental function based on feeding restrictions by the β phase or pore nucleation from the β phase. This suggests that a more complex multidimensional theory is required, by which both the beneficial and detrimental effects of iron on porosity formation can be explained. The development of this theory is the subject of two companion articles.[15,16]

V. CONCLUSIONS

1. Iron added deliberately to a commercial, unmodified, nongrain-refined Al-Si-Mg-Cu alloy (designated AA309) causes a threefold porosity effect that is dependent on both the concentration of iron and the prevailing solidification conditions. The three aspects of the effect are as follows.

   The overall porosity level decreases with iron content until a minimum value occurs at 0.4 pct Fe. As further iron additions are made, the overall porosity level increases.

   A change in pore morphology from discrete isolated pores to spongy interdendritic pores occurs even at small, deliberate additions of iron. These spongy regions become increasingly connected as the iron content increases above 0.4 pct.

   Under the poorest cooling and feeding conditions, increases in iron content above 0.4 pct lead to the development of a major, localized shrinkage defect.
2. Current theories regarding the deleterious role of iron on porosity formation are unable to explain the occurrence of a minimum in porosity at an intermediate iron level.

ACKNOWLEDGMENTS

Thanks are expressed to Comalco Aluminium Limited for the use of the ILP casting technology and to the Ford Motor Company of Australia Limited, whose industrial casting experiences have been used illustratively in this article. The Cooperative Research Centre for Alloy and Solidification Technology (CAST) was established under and is funded in part by the Australian Government's Cooperative Research Centre Scheme.

REFERENCES

1. D.R. Irani and V. Kondic: *AFS Trans.*, 1969, vol. 77, pp. 208-11.
2. H. Iwahori, K. Yonekura, Y. Yamamoto, and M. Nakamura: *AFS Trans.*, 1990, vol. 98, pp. 167-73.
3. J. Campbell: *Castings*, Butterworth Heinemann, Oxford, United Kingdom, 1991, p. 191.
4. H. Shahani: *Scand. J. Metall.*, 1985, vol. 14, pp. 306-12.
5. G. Laslaz and P. Laty: *AFS Trans.*, 1991, vol. 99, pp. 83-90.
6. P.S. Mohanty, F.H. Samuel, and J.E. Gruzleski: *Proc. Int. Symp. on Light Metals Processing and Applications*, Canadian Institute of Mining, Metallurgy and Petroleum, Montreal, 1994, pp. 273-82.
7. D. Argo and J.E. Gruzleski: *AFS Trans.*, 1988, vol. 96, pp. 65-74.
8. G.K. Sigworth, C. Wang, H. Huang, and J.T. Berry: *AFS Trans.*, 1994, vol. 102, pp. 245-62.
9. N. Roy, P.R. Louchez, and F.H. Samuel: *J. Mater. Sci.*, 1996, vol. 31, pp. 4725-40.
10. J.A. Taylor: *Cast Met.*, 1995, vol. 8 (4), pp. 225-52.
11. H. Iwahori, H. Takamiya, K. Yonekura, Y. Yamamoto, and M. Nakamura: *Casting*, 1988, vol. 60 (9), pp. 590-95.
12. M. Claude Mascre: *Fonderie*, 1955, vol. 108, pp. 4330-36.
13. N. Roy, A.M. Samuel, and F.H. Samuel: *Metall. Mater. Trans. A*, 1996, vol. 27A, pp. 415-29.
14. J.A. Taylor: Ph.D. Thesis, The University of Queensland, Brisbane, Queensland, Australia, 1997.
15. J.A. Taylor, G.B. Schaffer, and D.H. StJohn: *Metall. Mater. Trans. A*, 1999, vol. 30A, pp. 1651-55.
16. J.A. Taylor, G.B. Schaffer, and D.H. StJohn: *Metall. and Mater. Trans. A*, 1999, vol. 30A, pp. 1657-62.
17. L. Anantha Narayanan, F.H. Samuel, and J.E. Gruzleski: *Metall. Mater. Trans. A*, 1994, vol. 25A, pp. 1761-73.
18. P. Villars and L. Calvert: *Pearson's Handbook of Crystallographic Data for Intermetallic Phases*, 2nd ed., ASM INTERNATIONAL, Materials Park, OH, 1991, vol. 1.
19. L. Mondolfo: *Aluminium Alloys: Structure and Properties*, Butterworth and Co., London, 1976.
20. J. Campbell: *Proc. 4th Asian Foundry Congr.*, Australian Foundry Institute, Queensland Division, Brisbane, Australia, 1996, pp. 33-50.
21. L. Backerud, G. Chai, and J. Tamminen: *Solidification Characteristics of Aluminum Alloys: Vol. 2—Foundry Alloys*, AFS/Skanaluminium, Des Plaines, IL, 1990, pp. 119-26.
22. R. Smythe: Ford Motor Company of Australia Ltd., Geelong, Victoria, Australia, private communication, 1994.
23. J.E. Eklund: Ph.D. Thesis, Helsinki University of Technology, Helsinki, Finland, 1993.